This is the Pre-Published Version.

This is the peer reviewed version of the following article: B. Ge, J. Deng, Z. Wang, Q. Liang, L. Hu, X. Ren, R. Li, Y. Lin, Y. Li, Q. Wang, B. Han, Y. Deng, X. Fan, B. Li, G. Chen, X. Yu, Aggregate-Dominated Dilute Electrolytes with Low-Temperature-Resistant Ion-Conducting Channels for Highly Reversible Na Plating/Stripping. Adv. Mater. 2024, 36, 2408161, which has been published in final form at https://doi.org/10.1002/adma.202408161. This article may be used for non-commercial purposes in accordance with Wiley Terms and Conditions for Use of Self-Archived Versions. This article may not be enhanced, enriched or otherwise transformed into a derivative work, without express permission from Wiley or by statutory rights under applicable legislation. Copyright notices must not be removed, obscured or modified. The article must be linked to Wiley's version of record on Wiley Online Library and any embedding, framing or otherwise making available the article or pages thereof by third parties from platforms, services and websites other than Wiley Online Library must be prohibited.

Aggregate-dominated dilute electrolytes with low-temperature-resistant ion-conducting channels for highly reversible Na plating/stripping

Bingcheng Ge[1,11], Jiaojiao Deng[2, 11], Zhijie Wang[3, 11], Qinghua Liang[4], Liang Hu[1], Xiuyun Ren[1], Runmin Li[5], Yuxiao Lin[5*], Yunsong Li[6], Qingrong Wang[7], Bin Han[7], Yonghong Deng[7], Xiulin Fan[8*], Baohua Li[9*], Guohua Chen[10*], Xiaoliang Yu[1*]

[1] Department of Mechanical Engineering and Research Institute for Smart Energy, The Hong Kong Polytechnic University, Hong Kong, China

[2] Graphene Composite Research Center, College of Chemistry and Environmental Engineering, Shenzhen University, Shenzhen, 518060 China

[3] Department of Applied Physics, The Hong Kong Polytechnic University, Hong Kong, China

[4] Key Laboratory of Rare Earth, Ganjiang Innovation Academy, Chinese Academy of Sciences, Ganzhou, Jiangxi, 341000 China

[5] School of Physics and Electronic Engineering, Jiangsu Normal University, Xuzhou, 221116 China

[6] Zhejiang Laboratory, Hangzhou, 311100 China

[7] Department of Materials Science and Engineering, School of Innovation and Entrepreneurship, Guangdong Provincial Key Laboratory of Energy Materials for Electric Power, Southern University of Science and Technology, Shenzhen, 518055 China

[8] State Key Laboratory of Silicon and Advanced Semiconductor Materials, School of Materials Science and Engineering, Zhejiang University, Hangzhou, China

[9] Tsinghua Shenzhen International Graduate School, Tsinghua University, Shenzhen, 518055 China

[10] School of Energy and Environment, City University of Hong Kong, Kowloon, Hong Kong, China

[11] These authors contributed equally: Bingcheng Ge, Jiaojiao Deng, Zhijie Wang

* Correspondence: xiaoliang.yu@polyu.edu.hk; guohchen@cityu.edu.hk; libh@sz.tsinghua.edu.cn; xlfan@zju.edu.cn; linyuxiaochris@126.com

Abstract

Developing rechargeable batteries with high power delivery at low temperatures (LT) below 0 °C is significant for cold-climate applications. Initial anode-free sodium metal batteries (AFSMBs) promise high LT performances because of the low de-solvation energy and smaller Stokes radius of Na^+, non-diffusion-limited plating/stripping electrochemistry, and maximized energy density. However, the severe reduction in electrolyte ionic conductivity and formation of unstable solid electrolyte interphase (SEI) hinder their practical applications at LT. In this study, a 2-methyltetrahydrofuran-based dilute electrolyte is designed to concurrently achieve an anion-coordinated solvation structure and impressive ionic conductivity of 3.58 mS cm^{-1} at −40 °C. The dominant aggregate solvates enable the formation of highly efficient and LT-resistant Na^+ hopping channels in the electrolyte. Moreover, the methyl-regulated electronic structure in 2-methyltetrahydrofuran induces gradient decomposition toward an inorganic-organic bilayer SEI with high Na^+ mobility, composition homogeneity, and mechanical robustness. As such, a record-high Coulombic efficiency beyond 99.9% is achieved even at −40 °C. The as-constructed AFSMBs sustain 300 cycles with 80% capacity maintained, and a 0.5-Ah level pouch cell delivers 85% capacity over 180 cycles at −25 °C. This study affords new insights into electrolyte formulation for fast ionic conduction and superior Na reversibility at ultralow temperatures.

1. Introduction

Li-ion batteries (LIBs) dominate the global energy storage market for portable electronics and electric vehicles because of their high energy/power density, long cycle life, and environmental friendliness[1,2]. However, severe performance decay occurs at low temperatures (LT) below 0 °C, representing a significant obstacle to their deployment in cold-climate applications, including aeronautics/space missions, polar expeditions, and various military and civil facilities[3]. The obvious energy and power loss at LT comes from the abruptly reduced electrolyte ionic conductivity, retarded interfacial charge transfer kinetics, and decelerated ion transport through the electrode-electrolyte interfaces and bulk electrodes[4,5]. Current LIB-powered devices mostly employ supplementary warming systems to guarantee optimal operation at LT, which inevitably reduces the energy density[6,7]. Developing novel energy storage systems with high power output at LT is highly desirable[8].

Rechargeable sodium batteries are emerging beyond-Li-ion battery technologies, in which the lower de-solvation energy and smaller Stokes radius of Na^+ provide more opportunities for achieving boosted LT performances[9,10]. Among various Na battery systems, initial anode-free sodium metal batteries (AFSMBs) coupling a bare anode current collector with a Na-containing cathode minimize the total electrode mass, thus enabling maximized energy densities comparable to LIBs[11]. The anode electrochemistry of Na plating/stripping is non-diffusion-limited[12], different from conventional diffusion-controlled intercalation[13], alloying[14], and conversion-based[15] electrochemistry, and favors further accelerated charge transfer kinetics at LT. Accordingly, AFSMBs are regarded among the most promising candidates for LT batteries with high energy output. Nevertheless, the severe ionic conductivity decrease at LT[16] and the formation of unstable solid electrolyte interphase (SEI)[17] cause uneven Na deposition. The Na plating/stripping Coulombic efficiency (CE) thus falls far below the 99.9+% required for sustainable AFSMB operation. As a result, the LT performances of most state-of-the-art AFSMBs remain impractical.

The electrolyte solvation structure is of critical importance in determining the LT ion conducting property and anodic interfacial reactions. Typically, the solvent-separated

ion pair (SSIP) solvate exhibits a robust Na^+-solvent coordination. The solvation shell remains essentially intact, allowing rapid movement of the Na^+-solvent complex in the electrolyte[18]. However, such smooth ion-conducting channels are sensitive to LT, with solvated Na^+ transport severely retarded by the strong intermolecular attraction[19]. The de-solvation kinetics are also impeded at LT, encouraging a greater number of solvent molecules to participate in the formation of organic-rich SEI[20]. Contact-ion pair (CIP) and aggregate (AGG) solvates involve anions in the solvation complex, which could reduce the de-solvation energy and induce anion-derived inorganic-rich species in electrode/electrolyte interphases[21]. Unfortunately, CIP/AGG-dominated electrolytes typically show sluggish Na^+ conduction. For instance, salt-concentrated electrolytes featuring percolated nanometric aggregates conduct Na^+ ions mainly through the hopping mechanism, yet the high viscosity limits the Na^+-ion conductivity at LT[22,23]. Non-solvating diluents, such as fluorinated ethers, disintegrate bulk AGG clusters into smaller AGGs and reduce/increase the viscosity/wettability, but the ion-conducting efficiency in the electrolytes is suboptimal[24,25]. Their hyperreactivity with Na metal also leads to low interfacial compatibility. Recently proposed weakly solvating electrolytes can facilitate fast desolvation and anion-tuned SEI for rapid Na^+ migration. But the low sodium-salt dissociation impedes rapid Na^+ transport in the electrolyte[17,26,27]; To date, concurrently achieving an anion-coordinated solvation structure and a high LT ionic conductivity is extremely challenging.

Recently, Fan and colleagues reported a groundbreaking work showcasing the great potential of small-sized fluoroacetonitrile solvent-based electrolytes with hybrid vehicular and structural ion transport (1:1) for achieving superior ionic conductivities [28]. The impact of cooling on the evolution of ion conduction mechanisms has not yet been clarified. In this work, a 2-methyltetrahydrofuran (MeTHF)-based dilute electrolyte with a weak dissociation of Na^+-PF_6^- ion pairs is developed to build highly reversible AFSMBs at LT. It breaks through the intermolecular attraction-induced LT ion-conducting limitation of conventional electrolytes. The LT-resistant ion conduction channels enable an impressively high ionic conductivity of 3.58 mS cm^{-1} at −40 °C. Furthermore, the small AGG-dominated solvation structure with methyl-regulated

electronic structure induces a gradient electrolyte decomposition into an inorganic-organic bilayer SEI with fast Na^+ transfer kinetics, composition homogeneity, and mechanical robustness. As a result, a record-high CE beyond 99.9% is achieved at an ultralow temperature of −40 °C, and an AFSMB sustains 300 cycles with an 80% capacity retention. A 0.5-Ah level pouch-type AFSMB delivers a lifespan of over 180 cycles with an 85% capacity retention at −25 °C, which is superior to most published results.

Results

Electrolyte screening for highly reversible AFSMBs at LT

The Na plating/stripping reversibility at LT is highly related to electrolytes' freezing properties, ion-pairing features, and decomposition pathways on Na anodes[17,28]. We first screened Na salts by balancing the ion-pairing level and solubility property (Fig. 1a, left). As summarized in Supplementary Fig. 1, sodium tetrafluoroborate ($NaBF_4$) exhibits the highest lattice energy, resulting in significant difficulty in salt solubility in the conventional cyclic ether such as MeTHF. Sodium triflate (NaOTf) and sodium hexafluorophosphate ($NaPF_6$) have similarly high lattice energies but distinctive solubility properties. NaOTf was slightly dissolved by MeTHF, while $NaPF_6$ shows a high solubility of >1 M, owing to the more favorable charge distribution of PF_6^- for easy dissolution. Sodium bis(fluorosulfonyl)imide (NaFSI) and sodium bis(trifluoromethylsulfonyl)imide (NaTFSI) with low lattice energies can be well dissolved in MeTHF. Yet, they were reported to show much poorer Na anode compatibility than $NaPF_6$[29,30], as confirmed by the Na reversibility tests (see Supplementary Fig. 2). As such, $NaPF_6$ is selected as the main salt in the electrolytes.

Cyclic ethers with low melting points, weak solvating power, and high Na metal compatibility were then selected for formulating proper LT electrolytes. Three primary indicators of a solvent's capacity to dissolve salts include Gutmann donor number (*DN*), dielectric constant (ε), and dipole moment (μ)[31-33], but their individual effects are ambiguous. As summarized in Supplementary Table 1, there appears to be no discernible correlation of the solvent's $NaPF_6$ solubility with *DN* but a significant

positive correlation with ε, except for 1,3-dioxolane (DOL). Upon careful consideration of the indicator μ, it can be observed that high $NaPF_6$ solubility demonstrates a strong correlation with both high values of ε and μ (Fig. 1a, middle). The electrolyte was thus formulated by dissolving $NaPF_6$ into MeTHF for investigation (denoted as MeTHF electrolyte), which may own high ionic conductivity, anion-coordinated solvation structure, and low-temperature resistance (Fig. 1a, right). A concentration of 0.8 M was determined because of its optimized electrochemical performance (see Supplementary Fig. 3). A strongly solvating electrolyte of 0.8 M $NaPF_6$ dissolving in a mixture of diethylene glycol dimethyl ether (G2) and anti-freezing 1,3-dioxolane (DOL) (~7:3 in volume and ~1.1:1 in mole) was prepared as the reference (denoted as G2/DOL electrolyte). Both electrolytes are anti-freezing, which is a prerequisite for LT battery applications (Supplementary Fig. 4).

The Na plating/stripping reversibility was investigated using Na||Al half cells. At room temperature (RT), the MeTHF electrolyte displays a high and stable Na plating/stripping CE of 99.8% at 0.5 mA cm^{-2} under a capacity of 1 mA cm^{-2}, close to that of the G2/DOL electrolyte (99.9%) (Supplementary Fig. 5). The G2/DOL electrolyte shows a gradually increasing CE until stabilization at a high level (~99.8%) at –25 °C, which however, fluctuated severely after 100 plating/stripping cycles and finally caused cell failure (Fig. 1b, top). In stark contrast, the MeTHF electrolyte demonstrates high and stable CE of beyond 99.9% only after 10 cycles, which maintains quite stable over prolonged 400 cycles. The corresponding voltage profiles do not exhibit any discernible difference over cycling (Supplementary Fig. 6). When the current density increases to 1.0 mA cm^{-2}, the CE value is still over 99.9% at –25 °C (Supplementary Fig. 7).

To further evaluate the LT operation capability of the MeTHF electrolyte, the Na reversibility at the temperature of –40 °C was investigated. The stable Na plating/stripping CE values at 0.5 mA cm^{-2} (Supplementary Fig. 8) and 1.0 mA cm^{-2} (Fig. 1b, bottom) were determined to be beyond 99.9% over 200 cycles. The Na plating/stripping reversibility was also estimated by the well-known Aurbach method[34]. The MeTHF electrolyte enables a CE beyond 99.9% at both –25 and –40 °C

(Supplementary Fig. S9). Such remarkable performance is far superior to state-of-the-art LT electrolytes, as summarized in Fig. 1c, including those THF/DOL-based weakly sovating electrolytes, especially considering the applied ultralow temperature of −40 °C.

Encouraged by the superior Na reversibility, we constructed AFSMB cells comprising a $Na_3V_2(PO_4)_3$ cathode (Supplementary Figs. 10-12) and a carbon-coated aluminium anode current collector. Galvanostatic cycling demonstrates a high initial discharge capacity of 94 mAh g^{-1} at RT. This value decreases by 6%, 36%, and 57% when the operation temperature is sequentially reduced to 0, –25, and –40 °C, respectively (Supplementary Fig. 13a). The CE value increases with reduced temperature, reaching 99.9% at –40 °C, indicating the superior reversibility of anode-free cells. Moreover, the capacity is well recovered as the temperature returns to room temperature. The charge-discharge curves show negligible voltage polarization and little depression with temperature stepping (Supplementary Fig. 13b), suggesting superior charge transfer kinetics. The long-term cycling stability of AFSMBs at LT was investigated with coin-type cells first. The anode-free cell with the MeTHF electrolyte delivers an initial discharge capacity of 82 mAh g^{-1} and maintains 80% of the capacity over 300 cycles at −25 °C (Fig. 1d). In contrast, the G2/DOL system shows a much lower initial capacity of 57.8 mAh g^{-1}, which retains only 75% over 300 cycles. When the temperature is further reduced to –40 °C, the G2/DOL system fails to operate (Supplementary Fig. 14); in sharp contrast, the MeTHF system can still stably run for 300 cycles with a high capacity retention of 78%.

To validate the feasibility of the MeTHF electrolyte in practical conditions, a 0.5-Ah-level pouch-type AFSMB was fabricated and tested using double-side-coated $Na_3V_2(PO_4)_3$ cathode films with high areal mass loading of ~30 mg cm^{-2}. The obtained charge-discharge voltage profiles at various current rates under −25 °C are illustrated in Supplementary Fig. 15. As the current rates increase from 0.1, 0.2 to 0.5 C, slight depression of the voltage plateaus can be observed, and high discharge capacities of 0.45, 0.42, and 0.38 Ah are delivered, respectively. The long-term cycling stability of the pouch cell at −25 °C is depicted in Fig. 1e. It maintains 95.5% of the initial capacity after cycling for 100 cycles at 0.2 C. It remains as high as 85% capacity at a higher

discharge rate of 0.5 C over the subsequent 80 cycles. Despite the need for optimization of cell fabrication parameters such as electrolyte amount in this research, such remarkable results have showcased the great potential of the MeTHF electrolyte for practical LT AFSMBs. The power delivery capability at LT of anode-free cells was further estimated based on the total mass of electrodes and current collectors. As summarized in Supplementary Table 2, the calculated energy density (219 Wh kg^{-1}) of the as-fabricated anode-free cell is over twice as large as that of the commercial $LiFePO_4$||graphite cell (100 Wh kg^{-1}) at −25 °C, revealing its superiority in LT energy output.

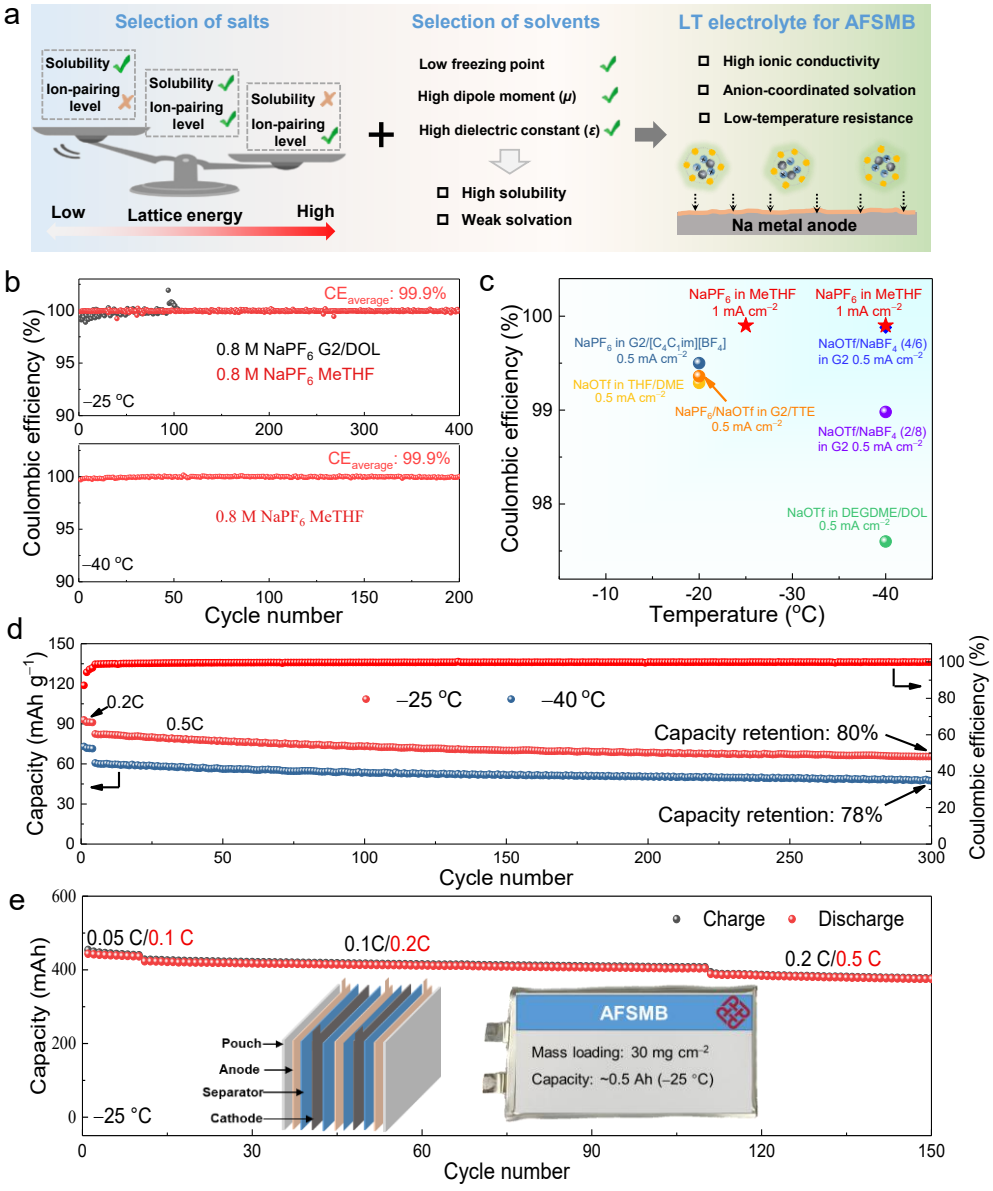

Fig. 1 | Electrolyte screening for high Na reversibility at LT. (**a**) Design principles

of LT electrolytes for AFSMBs. (**b**) Cycling stability of Na||Al half cells using MeTHF and G2/DOL electrolytes at 0.5 mA cm^{-2}/1 mAh cm^{-2} under −25 °C. (**c**) Comparison of LT Na plating/stripping CEs in the MeTHF electrolyte with those reported electrolytes[17,35-39]. (**d**) Long-term cycling performance of anode-free coin cells at 0.5 C under −25 and −40 °C. (**e**) Cyclability of the anode-free pouch cell at −25 °C. The inset is the optical image and configuration of the as-fabricated pouch cell.

Aggregate-dominated solvation structure

The solvation structures of electrolytes were studied using Raman spectroscopy and density functional theoretical (DFT) calculations. Fig. 2a displays the Raman spectra of investigated electrolytes and their components. A prominent fingerprint peak centred at 850 cm^{-1} can be detected in the G2 solvent, corresponding to the C−O stretching vibration. This characteristic peak was largely blue-shifted by ∼10 cm^{-1} in the G2/DOL electrolyte, indicating the strong coordination between the G2 solvent and Na^+. In contrast, the corresponding Na^+ coordination-derived blue shifts of MeTHF are much less noticeable owing to its weak binding with Na^+, as confirmed by lower binding energies of various Na^+-solvent complexes revealed by the DFT calculation (Supplementary Table 3).

The peak at 765 cm^{-1} is ascribed to the P–F symmetric stretch in $NaPF_6$, which shows a prominent red shift in three electrolytes due to largely reduced PF_6^--Na^+ coordination after dissociation[40]. A slight blue shift of this peak is observed from the G2/DOL electrolyte compared to the MeTHF electrolyte, indicating the existence of more PF_6^--Na^+ pairs. Based on the fitting results of the Raman spectra in Fig. 2b, the G2/DOL electrolyte shows an SSIP-dominated solvation structure (50.61% SSIP), while AGGs are dominant in the MeTHF electrolyte with a high content of 67.88%. Note that the SSIP proportion is determined to be less than 6%, which has rarely been reported in dilute electrolytes[23]. Importantly, the anion attributes greatly affect the ion-pairing level in the electrolyte solvates. As evidenced in Supplementary Figs. 16 and 17, when NaFSI or NaTFSI salt with much lower lattice energies is used, the SSIP ratio of the as-formulated electrolytes remarkably increases, but the AGG ratio decreases.

Molecular dynamics (MD) simulations were carried out to obtain a more detailed investigation of the solvation structures and Na^+ coordination environments. Many heterogeneously distributed and small-sized anion-cation-solvent clusters are observed in the MeTHF electrolyte (Fig. 2c) owing to the low solvation ability of MeTHF and the weak dissociation of Na^+-PF_6^- ion pairs. In contrast, the G2/DOL electrolyte shows a typical SSIP-dominant structure, with most anions uninvolved in the solvates (Fig. 2d). The radial distribution functions (RDF) and coordination numbers analysis confirm the significant involvement of anions in the primary solvation sheath of the MeTHF electrolyte and of solvents in that of the G2/DOL electrolyte (Fig. 2e, f), respectively. As the simulation temperature is reduced to an LT of 250 K, the small AGG-dominated solvation structure is maintained (Supplementary Figs. 18-20). And the theoretically quantified SSIP, CIP, and AGG content (Supplementary Fig. 21) agrees well with the Raman analysis. Note that the proportion of SSIP in the MeTHF electrolyte is negligibly small and thus is of minor consideration in the following discussions.

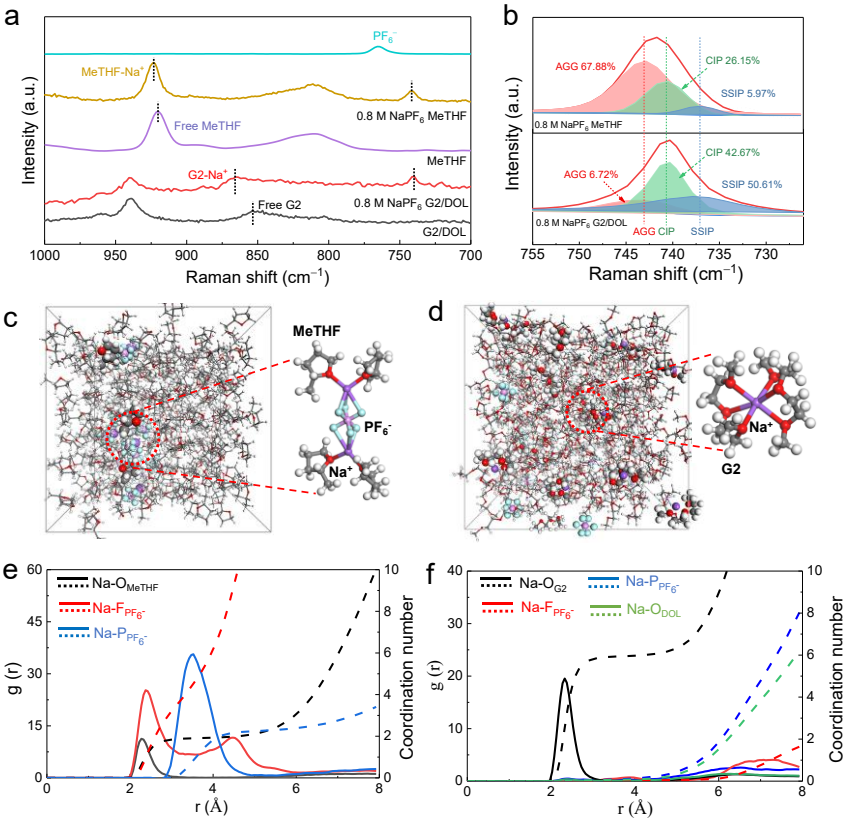

Fig. 2 | Experimental and theoretical analysis of electrolyte solvent structure. (**a**)

Raman spectra of the MeTHF and G2/DOL electrolytes and their components. (**b**) Fitted Raman spectra of PF_6^- anions for the MeTHF and G2/DOL electrolytes. Raman peaks from SSIP, CIP, and AGG solvates are located at 738.6, 741.7, and 743.8 cm^{-1}, respectively. Snapshots obtained from classical molecular dynamics simulations for the MeTHF (**c**) and G2/DOL (**d**) electrolytes. Na^+ radial distribution function (RDF) and coordination number in the MeTHF (**e**) and G2/DOL (**f**) electrolytes.

Low-temperature-resistant ion-conducting channels

A weak salt dissociation in electrolytes reduces the effective charge carrier density and ion-conducting capability[41,42]. We thus measured the ionic conductivities of the MeTHF and G2/DOL electrolytes at various temperatures. As shown in Fig. 3a, the weakly solvating MeTHF electrolyte exhibits an impressively high ionic conductivity of 5.53 mS cm^{-1} at RT, comparable to 6.25 mS cm^{-1} of the G2/DOL electrolyte. More importantly, the ionic conductivity maintains 3.58 mS cm^{-1} even at –40 °C, which is as high as 65% of the RT value. It is far superior to the G2/DOL and other reported MeTHF-based weakly solvating electrolytes[27,43,44], showcasing its excellence in LT ionic conduction. We determine the transference number (t_+) from the polarization curves (Supplementary Fig. 22). The MeTHF electrolyte shows a much higher t_+ value of 0.632 than the G2/DOL electrolyte (0.285). It suggests its high efficiency in conducting positive charge carriers, which is quite favorable for boosting the LT performance of AFSMBs[45].

Generally, the electrolyte viscosity derived from the intermolecular interaction of solvents impedes the charge carrier transfer[46]. In the viscosity-temperature curve (Fig. 3b), the G2/DOL electrolyte shows a higher room-temperature viscosity and a much more rapid increase with decreasing temperature than the MeTHF electrolyte. It can be ascribed to the small surface area of the cyclic ether MeTHF toward reduced dispersive forces[47]. The charge carrier mobilities (or diffusion coefficients) of investigated electrolytes at different temperatures were stimulated by tracking the mean-squared displacements (MSD) as a function of the time interval for 970 ps. As shown in Fig. 3c and Supplementary Fig. 23, the MeTHF electrolyte owns a much higher room-

temperature Na^+ diffusion coefficient of 4.65 $\times 10^{-10}$ m^2 s^{-1} than G2/DOL (2.83 $\times 10^{-10}$ m^2 s^{-1}). It remains 2.53 $\times 10^{-10}$ m^2 s^{-1} at –25 °C, which is over three times as high as the G2/DOL electrolyte (0.71 $\times 10^{-10}$ m^2 s^{-1}).

To understand the fast ion conducting mechanism, we performed MD simulations to investigate the molecular scale solvation dynamics and the anion/solvent residence time around the Na^+ cations, as shown in Fig. 3d-g and Supplementary Figs. 24, 25. The residence time of Na^+ in the MeTHF electrolyte is remarkably short, indicating frequent solvation of Na^+ by MeTHF molecules (approximately 134 ps at 300 K) and PF_6^- anions (approximately 332 ps at 300 K) (Fig. 3d). The highly rapid Na^+ hopping frequency between the neighboring coordination sites results in high ionic conductivity. Moreover, such Na^+-ion solvation environment does not significantly change as the temperature is reduced to 250 K, with slightly extended coordination periods of about 203 ps for MeTHF molecules and 390 ps for PF_6^- anions (Fig. 3e). In the G2/DOL electrolyte, G2 dominates the Na^+ solvation sheath because of its strong affinity to Na^+. Na^+ transfers through the vehicular mechanism, in which Na^+ is carried along by the solvation sheaths with a longer coordination period of about 490.8 ps at 300 K (Fig. 3f). Owing to the increasing viscosity, the residence time is extended to 1336.7 ps as the temperature is reduced to 250 K (Fig. 3g).

The energetic Na^+ hopping in the MeTHF electrolyte is also verified by the decreased activation energy of 0.48 eV compared to 1.08 eV of the G2/DOL electrolyte (Fig. 3h). Recall that the ratio of AGG/CIP solvates in the MeTHF electrolyte is about 3:1. The CIP solvates are in small sizes with low steric hindrance to migration. Therefore, they can serve as efficient intermediates for Na^+ hopping between adjacent AGG solvates (Fig. 3i). Such ion-conducting channels are preserved at LT for several reasons. First, the solvation structure of the MeTHF electrolyte is well maintained at LT. Second, the solvation/desolvation of Na^+ ions can easily occur at LT, enabling smooth Na^+ exchange between neighboring AGG and CIP solvates. Third, the increase in intermolecular attractions among solvates is negligible at reduced temperatures. In stark contrast, despite the rapid Na^+ conduction in the G2/DOL electrolyte at RT, the ion-conducting pathways are mostly blocked owing to the prominent intermolecular interactions. It has

been demonstrated that the presence of anions in the solvation sheaths promotes frequent hopping of cations[28]. Our results further highlight the necessity of maintaining an AGG-dominated solvation structure to achieve superior LT ionic conductivity. The observed rapid charge carrier transfer mechanism, primarily driven by AGG hopping, is substantiated by a notable reduction in ionic conductivity from 5.53 to 1.95 mS cm^{-1} as the salt concentration of $NaPF_6$-MeTHF electrolytes decreases from 0.8 to 0.5 M. The AGG content is significantly reduced from 68% to 27%, leading to a substantial decrease in the number of effective charge carriers and breaking of the ion-conducting network (Supplementary Figs. 27-29).

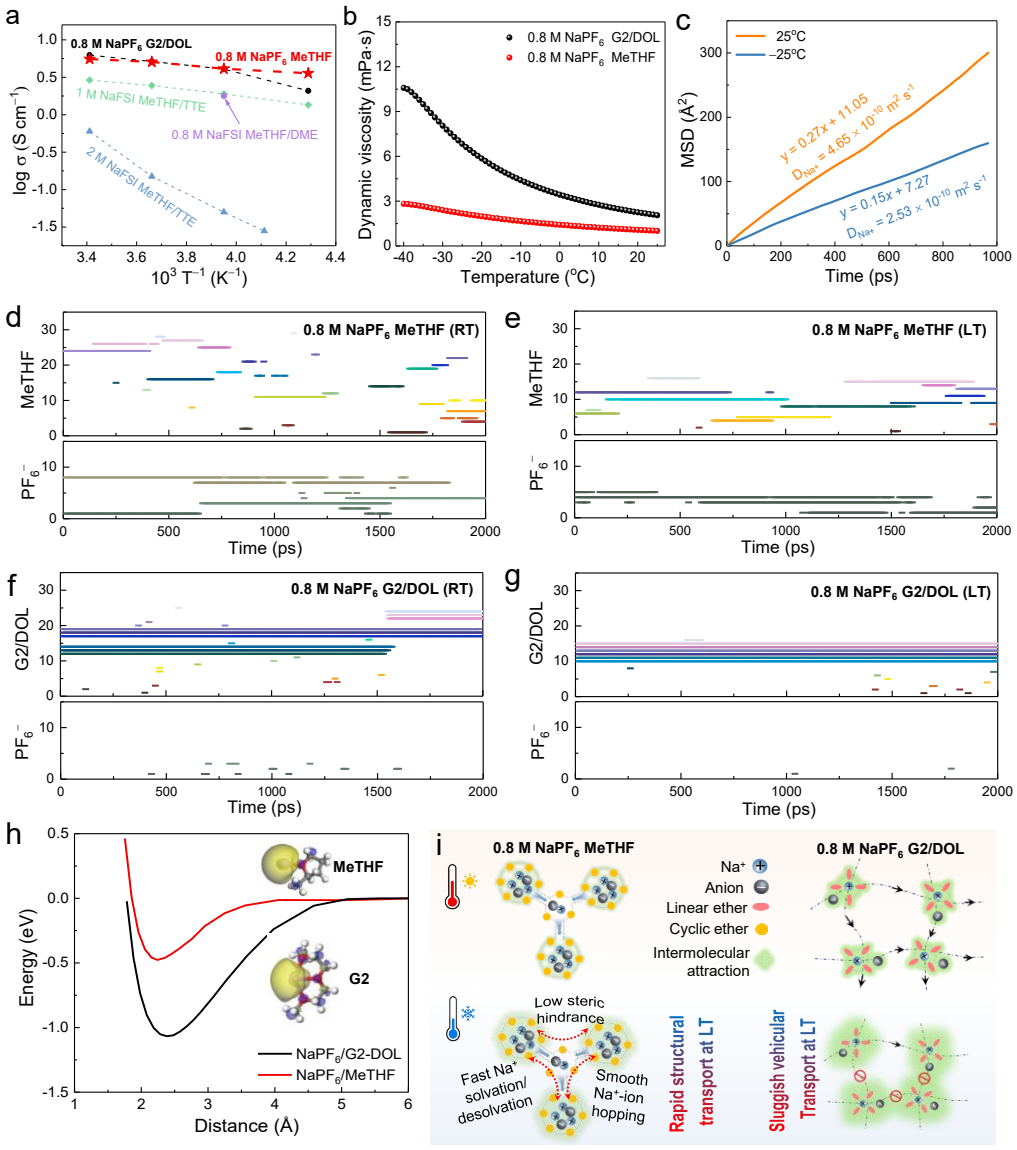

Fig. 3 | Physicochemical properties of investigated electrolytes. (**a**)Temperature-

dependent ionic conductivity of the MeTHF, G2/DOL, and other reported weakly solvating electrolytes. (**b**)Temperature-dependent viscosity of the MeTHF and G2/DOL electrolytes. (**c**) The mean-squared displacements of Na^+ in the MeTHF electrolyte at 25 °C and –25 °C. Evolution of Na-ion solvation environment in the MeTHF (**d, e**) and G2/DOL (**f, g**) electrolytes from molecular dynamics simulations at 300 K and 250 K (the vertical axis represents the serial number of different solvents or anions coordinated with the investigated Na^+ in the simulation time of 2,000 ps). (**h**) Variation of energy barrier of Na^+ hopping in the MeTHF and G2/DOL electrolytes. Insets, spatial distribution function of Na^+ ions around the MeTHF and G2 solvents. (**i**) Shematic illustrations of ion conducting channels in the MeTHF and G2/DOL electrolytes at RT and LT.

Mechanistic understanding of superior Na reversibility

The composition and microstructure of SEI could largely affect the interfacial stability and the Na plating/stripping reversibility[48]. Comprehensive and precise analysis of the SEI formation pathway, particularly the reduction sequence of electrolyte components at the Na anode interface, is critical for understanding the SEI structure[49,50]. Accordingly, DFT calculations were performed to evaluate their lowest unoccupied molecular orbital (LUMO) energy levels and Fukui functions. We found that the energy levels of free anions and solvents are much reduced after solvation (Supplementary Table 4). As illustrated in Fig. 4a, the small AGG solvate of $2Na^+$-$1PF_6^-$-4MeTHF and the SSIP solvate of Na^+-MeTHF own the lowest LUMO energy levels of –1.42 eV and –1.43 eV, respectively, predicting their preferential decomposition. The Fukui functions of the $2Na^+$-$1PF_6^-$-4MeTHF solvate in Supplementary Fig. 29 provide further insight into the electron density distributions around investigated atoms. The higher values around P and F atoms suggest higher electron density, thus favoring anion reduction to inorganic SEI species[51]. Considering the low SSIP proportion in the MeTHF electrolyte, we deduced that anion decomposition dominates its SEI formation process. Note that the methyl functional group plays a critical role in regulating the electronic structure of the solvent molecules and solvation complexes, thus changing the SEI formation

pathway. In the case of the 0.8 M $NaPF_6$ in THF electrolyte, the SSIP solvate of Na^+-THF exhibits a much lower LUMO energy level of –1.43 than –0.49 eV of the CIP solvate ($1Na^+$-$1PF_6^-$-3THF) and 0.03 eV of the small AGG solvate ($1Na^+$-$2PF_6^-$-2THF) (Supplementary Fig. 30), suggesting its preferential reduction to organic SEI species. This decomposition pathway is quite different from the MeTHF counterpart despite their similar small-AGG-dominated solvation structures (Supplementary Figs. 31-35). In the case of the G2/DOL electrolyte, the energy level gap between the SSIP solvate (Na^+-2G2, –0.65 eV) and CIP solvate (Na^+-PF_6^--G2, –0.01 eV) is not that prominent, allowing the simultaneous decomposition of solvents and anions to form an organic-inorganic hybrid structure.

To realize three-dimensional (3D) characterization and structural reconstruction of the SEI formed at LT, we carried out depth profile analyses of time-of-flight secondary ion mass spectrometry (ToF-SIMS). The NaF^- and C_2HO^- signals represent characteristic ionic fragments of NaF and organic components in SEI, respectively. We find that abundant C_2HO^- species exist at the surface of SEI formed in the MeTHF electrolyte (Supplementary Fig. 36a), which witnessed a fast reduction with sputtering. In contrast, the content of inorganic phases increases abruptly first and then decreases rapidly. It proves a bilayer structure with a surface organic layer and an internal inorganic layer, as illustrated in the 3D view (Fig. 4b). The SEI surface of the anode in the G2/DOL electrolyte shows a high content of both organic and inorganic species (Supplementary Fig. 36b). The C_2HO^- content gradually decreases with sputtering, and the inorganic content rises slightly and then gradually decreases, showing an organic-inorganic hybrid SEI structure (Fig. 4c). The THF electrolyte exhibits decreasing C_2HO^- content over sputtering with the inorganic content remaining low (Supplementary Figs. 37 and 38). It indicates an organic-dominated SEI structure that results in poor Na reversibility, which accords well with the above DFT simulations (Supplementary Fig. 39).

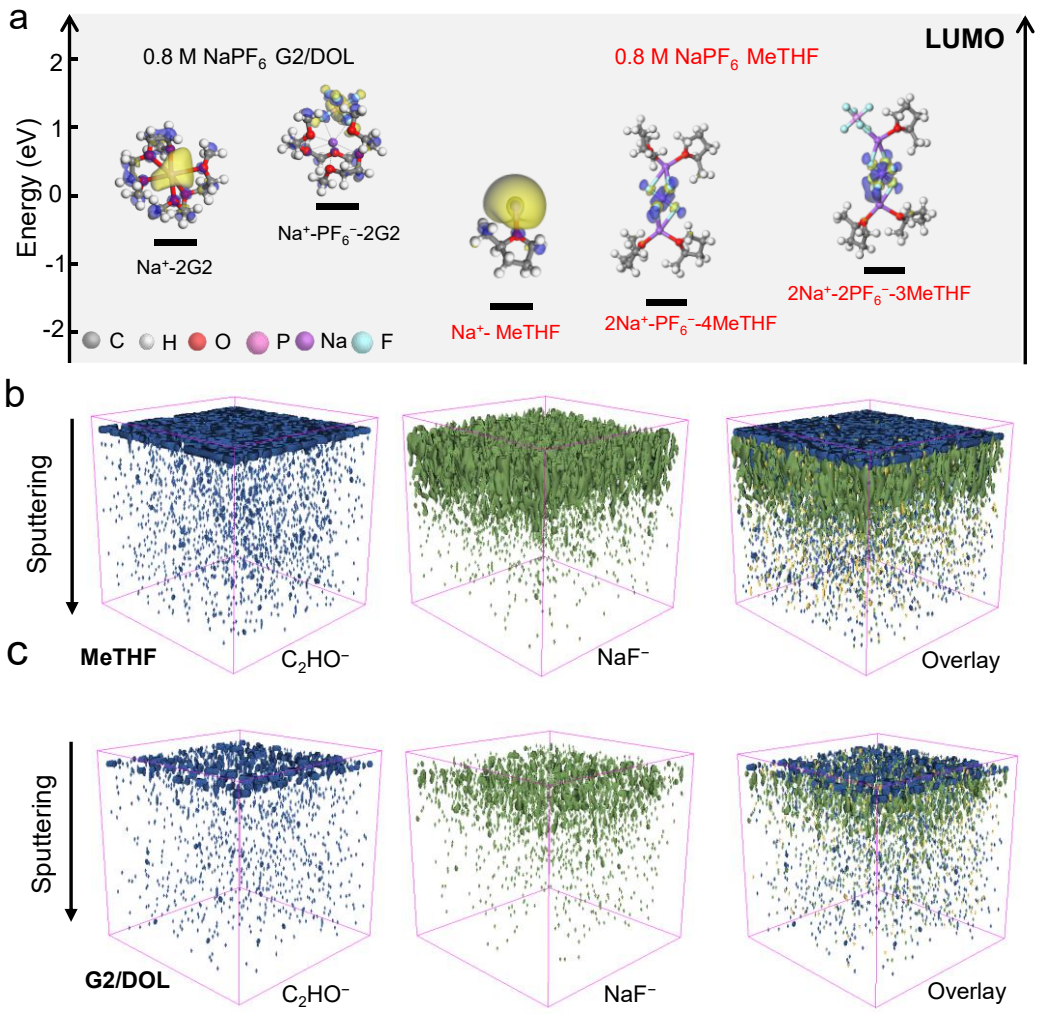

Fig. 4 | Formation pathway and structural characterization of SEI. (**a**) LUMO energy levels of solvation complexes of interest in the MeTHF and G2/DOL electrolytes. 3D rendering for the C_2HO^-, NaF^- secondary ions and the overlay in the ToF-SIMS tested for the SEI formed in the MeTHF (**b**) and G2/DOL (**c**) electrolytes at –25 °C.

The above-mentioned nanostructure of SEI was further validated by cryo-transmission electron microscopy (cryo-TEM). The MeTHF electrolyte-derived SEI shows a typical bilayer structure with a thin organic film (~5 nm) at the surface and a thick inorganic layer (~30 nm) in the interior (Fig. 5a, b). The crystalline nature of the inorganic SEI component corresponds to Na_2O, Na_2CO_3, and NaF through the lattice fringe analysis. The G2/DOL system-derived SEI exhibits a typical organic-inorganic hybrid structure (Fig. 5d, e). To obtain more detailed information on the electronic states

and distribution of SEI components, X-ray photoelectron spectroscopy (XPS) with in-depth Ar^+ sputtering was carried out. The surface of the SEI formed in the MeTHF electrolyte shows a strong C-C/C-H peak centred at 284.8 eV in the fitted C 1s spectrum (Supplementary Fig. 40a) and a moderate-intensity Na-F peak at 684.27 eV in the F 1s spectrum, which is reported to be ascribed to PO_yF_z-containing organic species (Supplementary Fig. 40b)[52]. An abrupt decrease in the C-C/C-H peak intensity is observed after sputtering for 8 seconds, which then continuously decreases over prolonged sputtering. This observation confirms the existence of a thin organic layer at the surface. In contrast, the intensity of the Na-F peak gradually increases due to the appearance of the interior inorganic layer. As for the G2/DOL system, the intensities of the C signal and F signal decreased simultaneously (Supplementary Fig. 41), which is the typical characteristic of an organic-inorganic hybrid SEI structure. Based on the results of ToF-SIMS, cryo-TEM, and XPS testing, we conclude the formation of a bilayer SEI structure with a compact organic-rich exterior and inorganic Na_2O/NaF-rich interior in the MeTHF electrolyte.

The reversibility of Na plating/stripping is highly correlated with the mechanical and Na^+-diffusion properties of the SEI. To evaluate the mechanical properties of the as-produced SEI, atomic force microscopy (AFM) measurement was performed (Fig. 5c, f and Supplementary Fig. 42). The average Young's modulus of SEI formed in the MeTHF electrolyte was 10.8 and 6.2 GPa at RT and –25 °C, respectively, much higher than those of the G2/DOL counterpart (8.5 and 4.3 GPa). Such mechanical strength enhancement is attributed to the rich NaF component in the inner layer, which owns a high Young's modulus of 76 GPa[53]. It effectively suppresses the growth and penetration of dendrites, thereby promoting enhanced reversibility of the Na anode. Moreover, the plated Na metal in the MeTHF electrolyte (Fig. 5c) displays a notably smoother morphology with a surface roughness of 37.6 nm than the G2/DOL electrolyte with a surface roughness of 45.2 nm (Fig. 5f). The morphology of plated Na metal was also observed by scanning electron microscopy (SEM), which shows dense, uniform, and dendrite-free sodium deposits in the MeTHF electrolyte at both –25 and −40 °C (Supplementary Fig. 43a, b). In contrast, sharp cracks and uneven deposit pits appear

in the G2/DOL system owing to the unstable SEI and 'dead' Na formation even at −25 °C (Supplementary Fig. 43c, d).

High interfacial exchange current density (j_0) is reported to be essential for achieving highly reversible Na plating/stripping[54]. The j_0 values of MeTHF and G2/DOL electrolytes were evaluated by linear fitting of Tafel plots at various temperatures (Supplementary Fig. 44). As shown in Fig. 5g, the G2/DOL system exhibits a high j_0 value of 2.07 mA cm^{-2} at 25 °C but maintains only 0.12 mA cm^{-2} at –40 °C. The MeTHF electrolyte manifests a similar room-temperature j_0 value of 1.53 mA cm^{-2} and remains as high as 0.56 mA cm^{-2} even at –40 °C, thus affording sufficient Na^+ ions beneath SEI to participate in the interfacial redox reaction. Based on the theoretical calculations as well as structural and electrochemical measurements, we anticipate that the superior LT Na reversibility is ascribed to the small aggregated dominated electrolyte with highly efficient and LT-resistant ion-conducting channels and the derived composition-homogenous, high-strength, and highly Na^+-conducting SEI (Fig. 5h). It is superior to the conventional SSIP-dominated electrolyte with LT-sensitive Na^+-conduction pathway and derived organic-inorganic hybrid SEI (Fig. 5i).

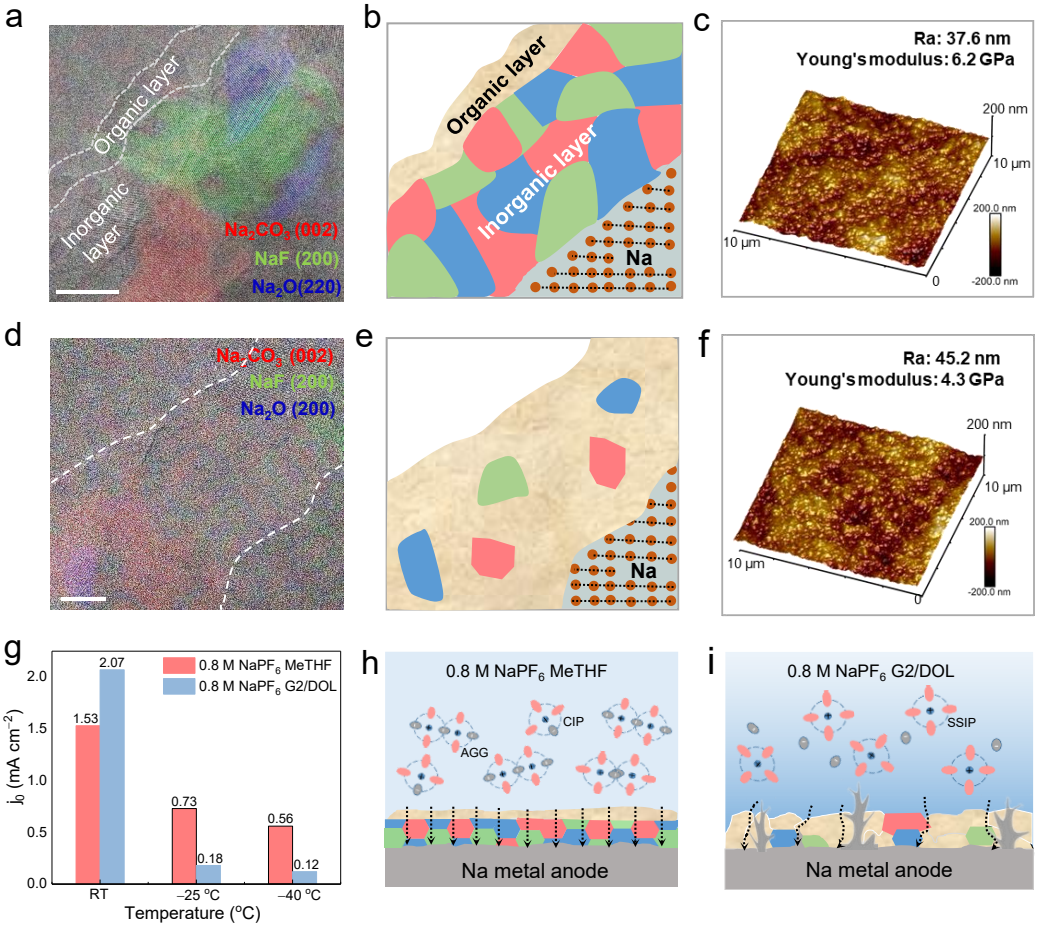

Fig. 5 | Physicochemical properties of SEI. Cryo-TEM images and the schematic illustrations of the SEI after cycling at −25 °C for the MeTHF (**a**, **b**) and G2/DOL (**d**, **e**) electrolytes. Scale bars, 10 nm. AFM surface profiling of SEI formed in the MeTHF (**c**) and G2/DOL (**f**) electrolytes at −25 °C. (**g**) Exchange-current densities (j_0) calculated from Tafel plots. Schematic illustration of the SEI structures formed in the MeTHF (**h**) and G2/DOL (**i**) electrolytes.

Discussion

In summary, we have designed a MeTHF-based dilute electrolyte to achieve a superior ionic conductivity of 3.58 mS cm^{-1} and beyond 99.9% Na plating/stripping Coulombic efficiency even at −40 °C. The as-formulated electrolyte shows a weak dissociation of Na^+-PF_6^- ion pairs but highly efficient Na^+ conducting channels. The AGG/CIP (~3:1 ratio) dominated solvation structure helps form an effective network for ultrafast Na^+ hopping. Intriguingly, such solvation structure is well preverved at LT and breaks through the intermolecular attraction-induced LT ion-conducting limitation of

conventional electrolytes. The LT-resistant ion-conducting channels assure smooth charge carrier transfer at reduced temperatures. Moreover, the well-regulated electronic structure by the methyl functional group enables preferential anion-decomposition to form a favorable bilayer SEI consisting of an inorganic interior and an organic surface, revealed by theoretical simulations and ToF-SIMS, XPS, cryo-TEM, AFM characterizations. It affords uniform Na^+ conduction channels for even Na deposition and high mechanical strength to inhibit Na dendrite growth. The as-constructed AFSMB cells sustain 300 cycles with 80% capacity maintained. A 0.5-Ah level anode-free pouch cell delivers 85% of the first discharge capacity over 180 cycles at −25 °C. Findings will be of immediate benefit for the design of long-life and high-performance AFSMBs at LT. The electrolyte design principles in this work can also be extended to other LT battery systems.

Methods

Materials

Battery-grade sodium bis(fluorosulfonyl)imide (NaFSI), sodium bis(trifluoromethylsulfonyl)imide (NaTFSI), sodium trifluoromethanesulfonate (NaOTf), sodium hexafluorophosphate ($NaPF_6$), sodium tetrafluoroborate ($NaBF_4$) were ordered from DodoChem and dried for over 12 hours in an argon-filled glovebox (Braun, O_2 <0.5 ppm, H_2O <0.1 ppm) before use. 2-methyltetrahydrofuran (MeTHF, anhydrous, $H_2O < 30$ ppm), tetrahydrofuran (THF, anhydrous, $H_2O < 50$ ppm), diethylene glycol dimethyl ether (G2, anhydrous, $H_2O < 50$ ppm), and 1,3-dioxolane (DOL, anhydrous, $H_2O < 30$ ppm) were purchased from Sigma-Aldrich and dried by using 4 Å molecular sieves before use. Metallic Na chips (average thickness of 0.5 mm) were fabricated by roll-pressing Na metal cubes (99.9% trace metals basis, Sigma-Aldrich) in the glove box, and the oxidized surfaces were removed using a knife.

To fabricate the $Na_3V_2(PO_4)_3$ cathode film, $Na_3V_2(PO_4)_3$ powder (Hubei Energy Tech. Co., Ltd.), acetylene black (Alfa Aesar Co., Ltd.), and polyvinylidene fluoride (PVDF, MTI Co., Ltd.) were mixed and homogenized using N-methyl pyrrolidinone (NMP, anhydrous, Sigma Aldrich) at a weight ratio of 90:5:5, And then spread the resulting

slurry onto the carbon-coated aluminum foil (99.9% purity, 16 μm thickness, MTI) using a doctor blade, dried at 120 °C for 6 hours in a blast oven and subsequently at 120 °C for 12 hours in a vacuum oven. The cathode films were then prepared by punching discs (Φ12 mm, active material loading of ~ 7 mg cm^{-2}) for coin-type cells or rectangles (12.1 cm × 6.1 cm, double-layer coating, active material loading of ~ 30 mg cm^{-2}) for pouch-type cells.

Physicochemical characterizations

Viscosities of electrolytes were measured using a Haake Mars 60 rheometer, specifically calibrated for LT measurements. Raman tests were performed using a micro-laser confocal Raman spectrometer (Horiba LabRAM HR800, France) with a 532 nm laser. The morphology of Na anodes was examined using scanning electron microscopy (SEM, Tescan VEGA3). The surface properties of as-obtained sodium anodes were investigated by X-ray photoelectron spectroscopy (XPS, PHI5000 VersaProbe II XPS with Al K irradiation of 1,486.6 eV) and time-of-flight secondary ion mass spectroscopy (ToF-SIMS, ULVAC-PHI, Japan, equipped with bismuth as primary ion source and Ar^- ion as sputter source). The surface fluctuation and Young's modulus of the obtained solid electrolyte interphase (SEI) were characterized by atomic force microscopy (AFM, Bruker, Dimension Icon) in an Ar-filled glovebox (O_2 <1 ppm, H_2O <0.1 ppm). AFM mapping was performed using the PeakForce tapping mode, and quantitative nanomechanics mode, along with the Derjaguin-Muller-Toropov model, was employed to determine the modulus. For all SEM/XPS/ToF-SIMS/AFM measurements, Na anodes in the charged state were used for characterization. Atomic imaging of SEI was obtained using cryo-transmission electron microscopy (cryo-TEM, a Krios G3i). All cryo-TEM images were captured at a temperature of 77 K while applying a low electron dose. To avoid contamination from air exposure, the samples for these tests were transferred with specially designed vessels.

Electrochemical measurements

Electrochemical tests were carried out using CR2025-type coin cells. The separator comprised a Whatman glass fibre sandwiched between two Celgard 2500 films. Na||Na

symmetric cells were assembled using two identical Na metal foils (ϕ14 mm). Na||Al and Na|| $Na_3V_2(PO_4)_3$ cells were fabricated by pairing a Na metal foil with an Al/C (ϕ 16 mm) and $Na_3V_2(PO_4)_3$ foil, respectively. Anode-free cells were constructed by pairing an $Na_3V_2(PO_4)_3$ cathode foil with an Al/C foil at the anode side. Pouch cells were assembled by pairing two double-layer-coated $Na_3V_2(PO_4)_3$ cathode films with three layers of Al/C foils and sandwich-structured separators soaked in the MeTHF electrolyte, followed by packaging with Al-plastic films. The cycling test of Na||Al cells was performed between 0 and 1 V versus Na/Na^+ with the Coulombic efficiency (CE) defined as the stripped/plated capacity ratio. Initial five activation charge-discharge cycles at 50 μA cm^{-2} were used to remove the surface contamination. For the Aurbach CE test, a standard protocol was followed. Initially, 5.0 mAh cm^{-2} of Na was deposited onto the Al/C foil at 0.5 mA cm^{-2}, then fully stripped to 1.0 V to form the SEI. Subsequently, 5.0 mAh cm^{-2} of Na was plated onto the substrate, followed by repeated Na stripping/plating cycles at a constant capacity of 1.0 mAh cm^{-2} and a current density of 0.5 mA cm^{-2} for 10 cycles. Finally, the cells were charged to 1.0 V.

The ionic conductivities of electrolytes were assessed by assembling symmetric stainless-steel cells using the following equation:

$$\delta = \frac{L}{A \times R},$$

where R is the ohmic resistance, A is the area, and L is the space between two stainless steel electrodes, respectively. The ohmic resistance was measured by AUTOLAB electrochemical station (NOVA) in the frequency range of 1.0 MHz to 10 mHz. The transference numbers were determined through the potentiostatic polarization tests of Na||Na cells based on the following equation:

$$t_+ = \frac{I_{SS}\,(\Delta V - I_0 R_0)}{I_0\,(\Delta V - I_{SS} R_{SS})},$$

where ΔV is the applied bias voltage, I_0 is the initial current, I_{SS} is the steady-state current, R_0 is the initial impedance, and R_{SS} is the steady-state impedance.

Computations

The solvation structures of electrolytes were calculated by molecular dynamics (MD) simulations. An amorphous simulation cell with randomly packed salt and solvent

molecules at a specific ratio was first constructed. Then, it was optimized using the CompassII force field and subjected to two classical MD simulations sequentially, i.e., an NPT (constant pressure and temperature) ensemble under 1 atm and an NVT (constant volume and temperature) ensemble[55]. The times for NPT and NVT simulation are 1 ns and 2 ns, respectively. The timestep was set to be 1 fs. The temperature was controlled by Nosé algorithm, and the pressure was regulated by the Berendsen algorithm[56]. The Ewald summation method was used for the electrostatic and the van der Waals interaction with an accuracy of 1×10^{-4} kcal mol^{-1} and a buffer width of 0.5 Å. The radial distribution function and coordination number were determined based on the data obtained from the final 1.0 ns of the NVT simulation. The diffusion coefficient was calculated based on the mean square displacement (MSD):

$$D = \frac{1}{6N_a} \lim_{\tau \to \infty} \frac{d}{d\tau} \sum_{t=0}^{t-\tau} \sum_{i}^{N_a} [r_i(t+\tau) - r_i(t)]^2 = \frac{1}{6} \lim_{\tau \to \infty} \frac{d}{d\tau} MSD(\tau)$$

where t is the simulation time, τ is the time interval, N_a is the total number of atoms in given species, $r_i\,(t+\tau)$ and $r_i\,(t)$ are the position vectors of atom i at different time ($t+\tau$ and t). To calculate the residence time, the coordinatio environment of the specific Na-ion in each frame of NVT simulation was analyzed. All the classical MD simulations were performed using the Forcite module in Materials Studio.

Density functional theory (DFT) calculations were conducted using the Dmol3 module in Materials Studio[57]. These calculations encompassed all electrons and employed a local basis set of Double Numerical plus Polarization (DNP). The exchange-correlation effects were accounted for using the Perdew-Burke-Ernzerhof (PBE) functional within the generalized gradient approximation (GGA)[58]. All ion positions were relaxed during energy minimization until one of the three convergence criteria, namely 3×10^{-4} eV/system for energy change, 0.05 eV/Å for force, and 0.005 Å for displacement, was met[59]. The COSMO solvation model was applied in all DFT calculations, wherein the solvent was treated as a dielectric continuum, and the dielectric constant was set to 7.2[60]. The Van Der Waals Interactions were corrected under the Tkatchenko-Scheffler (TS) scheme.

Data availability

The data supporting the findings of this study are available from the authors upon reasonable request.

References

1. Li, M., Lu, J., Chen, Z. & Amine, K. 30 years of lithium-ion batteries. *Adv. Mater.* **30**, 1800561 (2018).
2. Grey, C. P. & Hall, D. S. Prospects for lithium-ion batteries and beyond—a 2030 vision. *Nat. Commun.* **11**, 6279 (2020).
3. Gupta, A. & Manthiram, A. Designing advanced lithium-based batteries for low-temperature conditions. *Adv. Energy Mater.* **10**, 2001972 (2020).
4. Hubble, D. *et al.* Liquid electrolyte development for low-temperature lithium-ion batteries. *Energ. Environ. Sci.* **15**, 550-578 (2022).
5. Piao, N. *et al.* Challenges and development of lithium-ion batteries for low temperature environments. *eTransportation* **11**, 100145 (2022).
6. Wang, C.-Y. *et al.* Lithium-ion battery structure that self-heats at low temperatures. *Nature* **529**, 515-518 (2016).
7. Wu, W. *et al.* A critical review of battery thermal performance and liquid based battery thermal management. *Energ. Convers. Manage.* **182**, 262-281 (2019).
8. Holoubek, J. *et al.* Tailoring electrolyte solvation for Li metal batteries cycled at ultra-low temperature. *Nat. Energy* **6**, 303-313 (2021).
9. Li, Y. *et al.* Ether-based electrolytes for sodium ion batteries. *Chem. Soc. Rev.* **51**, 4484-4536 (2022).
10. Hu, Y.-S. & Pan, H. Solvation structures in electrolyte and the interfacial chemistry for Na-Ion batteries. *ACS Energy Lett.* **7**, 4501-4503 (2022).
11. Yang, T., Luo, D., Liu, Y., Yu, A. & Chen, Z. Anode-free sodium metal batteries as rising stars for lithium-ion alternatives. *iScience* **26**, 105982 (2023).
12. Wang, Y. *et al.* Developments and perspectives on emerging high-energy-density sodium-metal batteries. *Chem* **5**, 2547-2570 (2019).
13. Wang, Z. *et al.* Probing the energy storage mechanism of quasi-metallic Na in hard carbon for sodium-ion batteries. *Adv. Energy Mater.* **11**, 2003854 (2021).
14. Fang, L. *et al.* Conversion-alloying anode materials for sodium ion batteries. *Small* **17**, 2101137 (2021).
15. Li, Z. *et al.* Reacquainting the electrochemical conversion mechanism of FeS2 sodium-ion batteries by operando magnetometry. *J. Am. Chem. Soc.* **143**, 12800-12808 (2021).
16. Yang, S., Cheng, K. & Cao, Z. Status and strategies of electrolyte engineering for low-temperature sodium-ion batteries. *J. Mater. Chem. A* (2024).
17. Wang, C. *et al.* Extending the low-temperature operation of sodium metal batteries combining linear and cyclic ether-based electrolyte solutions. *Nat. Commun.* **13**, 4934 (2022).
18. Yang, X., Ji, M., Zhang, C., Yang, X. & Xu, Z. Physical insight into the entropy-driven ion association. *J. Comput. Chem.* **43**, 1621-1632 (2022).
19. Chen, X. *et al.* Dominant solvent-separated ion pairs in electrolytes enable

superhigh conductivity for fast-charging and low-temperature lithium ion batteries. *ACS Nano* **18**, 8350-8359 (2024).
20. Wu, H., Jia, H., Wang, C., Zhang, J.-G. & Xu, W. Recent progress in understanding solid electrolyte interphase on lithium metal anodes. *Adv. Energy Mater.* **11**, 2003092 (2021).
21. Li, Y., Bai, F., Li, C., Wang, Y. & Li, T. Understanding the inorganic-rich feature of anion-derived solid electrolyte interphase. *Adv. Energy Mater.*, 2304414 (2024).
22. Yu, Z. *et al.* Beyond local solvation structure: nanometric aggregates in Battery electrolytes and their effect on electrolyte properties. *ACS Energy Lett.* **7**, 461-470 (2022).
23. Hu, J. *et al.* Influence of electrolyte structural evolution on battery applications: Cationic aggregation from dilute to high concentration. *Aggregate* **3**, e153 (2022).
24. Cao, R. *et al.* Enabling room temperature sodium metal batteries. *Nano Energy* **30**, 825-830 (2016).
25. Fang, W. *et al.* Stable sodium metal anode enhanced by advanced electrolytes with SbF3 additive. *Rare Metals* **40**, 433-439 (2021).
26. Wang, S., Zhang, X.-G., Gu, Y., Tang, S. & Fu, Y. An ultrastable low-temperature Na metal battery enabled by synergy between weakly solvating solvents. *J. Am. Chem. Soc.* **146**, 3854-3860 (2024).
27. Fang, H. *et al.* Regulating ion-dipole interactions in weakly solvating electrolyte towards ultra-low temperature sodium-ion batteries. *Angew. Chem. Int. Ed.* **63**, e202400539 (2024).
28. Lu, D. *et al.* Ligand-channel-enabled ultrafast Li-ion conduction. *Nature* **627**, 101-107 (2024).
29. Ponrouch, A., Marchante, E., Courty, M., Tarascon, J.-M. & Palacín, M. R. In search of an optimized electrolyte for Na-ion batteries. *Energ. Environ. Sci.* **5**, 8572-8583 (2012).
30. Seh, Z. W., Sun, J., Sun, Y. & Cui, Y. A highly reversible room-temperature sodium metal anode. *ACS Cent. Sci.* **1**, 449-455 (2015).
31. Cheng, H. *et al.* High voltage electrolyte design mediated by advanced solvation chemistry toward high energy density and fast charging lithium-ion batteries. *Adv. Energy Mater.*, 2304321 (2024).
32. Xiao, P. *et al.* Insights into the solvation chemistry in liquid electrolytes for lithium-based rechargeable batteries. *Chem. Soc. Rev.* **52**, 5255-5316 (2023).
33. Yao, Y.-X. *et al.* Regulating interfacial chemistry in lithium-ion batteries by a weakly solvating electrolyte. *Angew. Chem. Int. Ed.* **60**, 4090-4097 (2021).
34. Su, L., Cui, Z. & Manthiram, A. Impact of high-nickel cathodes and test conditions on the coulombic efficiency of lithium metal in advanced electrolytes. *ACS Mater. Lett.* **6**, 109-114 (2024).
35. Zhou, J. *et al.* Low-temperature and high-rate sodium metal batteries enabled by electrolyte chemistry. *Energy Storage Mater.* **50**, 47-54 (2022).
36. Hu, X. *et al.* Deeply cycled sodium metal anodes at low temperature and in lean electrolyte conditions. *Angew. Chem. Int. Ed.* **60**, 5978-5983 (2021).

37. Thenuwara, A. C. *et al.* Enabling highly reversible sodium metal cycling across a wide temperature range with dual-salt electrolytes. *J. Mater. Chem. A* **9**, 10992-11000 (2021).
38. Liang, H.-J. *et al.* Ether-based electrolyte chemistry towards high-voltage and long-life Na-ion full batteries. *Angew. Chem. Int. Ed.* **60**, 26837-26846 (2021).
39. Zhu, Q. *et al.* A 110 Wh kg-1 Ah-level anode-free sodium battery at -40 ℃. *Joule* **8**, 482-495 (2024).
40. Morales, D., Ruther, R. E., Nanda, J. & Greenbaum, S. Ion transport and association study of glyme-based electrolytes with lithium and sodium salts. *Electrochim. Acta* **304**, 239-245 (2019).
41. Erben, D. *et al.* Excitation-induced transition to indirect band gaps in atomically thin transition-metal dichalcogenide semiconductors. *Phys. Rev. B* **98**, 035434 (2018).
42. Boz, B., Dev, T., Salvadori, A. & Schaefer, J. L. Review—electrolyte and electrode designs for enhanced ion transport properties to enable high performance lithium batteries. *J. Electrochem. Soc.* **168**, 090501 (2021).
43. Guo, D., Wang, J., Lai, T., Henkelman, G. & Manthiram, A. Electrolytes with solvating inner sheath engineering for practical Na–S batteries. *Adv. Mater.* **35**, 2300841 (2023).
44. Zhou, J. *et al.* Bulk bismuth anodes for wide-temperature sodium-ion batteries enabled by electrolyte chemistry modulation. *J. Colloid Interf. Sci.* **657**, 502-510 (2024).
45. Mönich, C., Andersson, R., Hernández, G., Mindemark, J. & Schönhoff, M. Seeing the unseen: Mg2+, Na+, and K+ transference numbers in post-Li battery electrolytes by electrophoretic nuclear magnetic resonance. *J. Am. Chem. Soc.* **146**, 11105-11114 (2024).
46. Wang, Y. *et al.* Weak solvent–solvent interaction enables high stability of battery electrolyte. *ACS Energy Lett.* **8**, 1477-1484 (2023).
47. Park, S.-J. & Seo, M.-K. Intermolecular force. *Interface Science and Technology* **18**, 1-57 (2011).
48. Bao, C. *et al.* Solid electrolyte interphases on sodium metal anodes. *Adv. Funct. Mater.* **30**, 2004891 (2020).
49. Takenaka, N., Bouibes, A., Yamada, Y., Nagaoka, M. & Yamada, A. Frontiers in theoretical analysis of solid electrolyte interphase formation mechanism. *Adv. Mater.* **33**, 2100574 (2021).
50. Xu, Y. *et al.* Promoting mechanistic understanding of lithium deposition and solid-electrolyte interphase (SEI) formation using advanced characterization and simulation methods: recent progress, limitations, and future perspectives. *Adv. Energy Mater.* **12**, 2200398 (2022).
51. Assat, G. & Tarascon, J.-M. Fundamental understanding and practical challenges of anionic redox activity in Li-ion batteries. *Nat. Energy* **3**, 373-386 (2018).
52. Schulz, N., Hausbrand, R., Wittich, C., Dimesso, L. & Jaegermann, W. XPS-surface analysis of SEI layers on Li-ion cathodes: Part II. SEI-composition and

formation inside composite electrodes. *J. Electrochem. Soc.* **165**, A833 (2018).
53. Gao, Y. *et al.* Critical roles of mechanical properties of solid electrolyte interphase for potassium metal anodes. *Adv. Funct. Mater.* **32**, 2112399 (2022).
54. Hobold, G. M. *et al.* Moving beyond 99.9% Coulombic efficiency for lithium anodes in liquid electrolytes. *Nat. Energy* **6**, 951-960 (2021).
55. Sun, H. *et al.* COMPASS II: extended coverage for polymer and drug-like molecule databases. *J. Mol. Model.* **22**, 47 (2016).
56. Nosé, S. A molecular dynamics method for simulations in the canonical ensemble. *Mol. Phys.* **52**, 255-268 (1984).
57. Delley, B. From molecules to solids with the DMol3 approach. *J. Chem. Phys.* **113**, 7756-7764 (2000).
58. Perdew, J. P., Burke, K. & Ernzerhof, M. Generalized gradient approximation made simple. *Phys. Rev. Lett.* **77**, 3865-3868 (1996).
59. Karasawa, N. & Goddard, W. A., III. Acceleration of convergence for lattice sums. *J. Phys. Chem. C* **93**, 7320-7327 (1989).
60. Klamt, A. & Schüürmann, G. COSMO: a new approach to dielectric screening in solvents with explicit expressions for the screening energy and its gradient. *J. Chem. Soc. Perk. T. 2*, 799-805 (1993).

Acknowledgements

The authors gratefully acknowledge financial support from National Natural Science Foundation of China (Nos. 52261160384 and 52072208), Natural Science Foundation of Guangdong (No. 2023A1515010020), Innovation and Technology Fund (ITS-325-22FP), Shenzhen Science and Technology Program (KJZD20230923114107014), the Guangdong Basic and Applied Basic Research Foundation (No. 2020A1515110798), Natural Science Fund for Colleges and Universities in Jiangsu Province (No. 22KJB430004), and Jiangsu Special Term Professor Program. Q. L. thanks the financial support fromNatural Science Foundation of Jiangxi (No. 20232ACB214001) and Research fund from the Chinese Academy of Sciences,

Author contributions

B. G., J. D., Z. W., G. C., X. Y. conceived the idea and designed this work. B. G., L. H., X. R. carried out the electrolyte regulation and electrochemical measurements. R. L., Y. L., Y. L. carried out the electrolyte regulation and electrochemical measurements; Q. W., B. H., Y. D. carried out the cryo-TEM characterizations and analysis; B. G., Y. L., X. F., B. L., G. C., X. Y. wrote the manuscript and participated in the discussion to

improve the paper. All authors endorsed the final version of the manuscript.

Competing interests

The authors declare no competing interests.

Additional information

The online version contains supplementary material available at